

Connecting multi-lepton anomalies at the LHC and in Astrophysics with MeerKAT/SKA

Geoff Beck,^{1*} Ralekete Temo,¹ Elias Malwa,² Mukesh Kumar,² and Bruce Mellado,^{2,3}

¹*School of Physics and Centre for Astrophysics, University of the Witwatersrand, Johannesburg, Wits 2050, South Africa.*

²*School of Physics and Institute for Collider Particle Physics, University of the Witwatersrand, Johannesburg, Wits 2050, South Africa.*

³*iThemba LABS, National Research Foundation, PO Box 722, Somerset West 7129, South Africa.*

Accepted XXX. Received YYY; in original form ZZZ

ABSTRACT

Multi-lepton anomalies at the Large Hadron Collider (LHC) are reasonably well described by a two Higgs doublet model with an additional singlet scalar. Here we demonstrate that using this model, with parameters set by the LHC, we are also able to describe the excesses in gamma-ray flux from the galactic centre and the cosmic-ray spectra from AMS-02. This is achieved through Dark Matter (DM) annihilation via the singlet scalar. Of great interest is the flux of synchrotron emissions which results from annihilation of DM in Milky-Way satellites. We make predictions for MeerKAT/SKA observations of the nearby dwarf galaxy Reticulum II and we demonstrate the power of this instrument as a new frontier in indirect dark matter searches. Since the dark matter sector of the aforementioned two Higgs doublet model is unconstrained by current LHC data, we also demonstrate a synergy between particle and astrophysical searches in order to motivate further exploration of this promising model.

Key words: dark matter – radio continuum: general – astroparticle physics

1 INTRODUCTION

The discovery of a Higgs boson (h) (Higgs 1964a; Englert & Brout 1964; Higgs 1964b; Guralnik et al. 1964) at the Large Hadron Collider (LHC) by the ATLAS (Aad et al. 2012) and CMS (Chatrchyan et al. 2012) experiments has opened a new chapter in particle physics. Measurements provided so far indicate that the quantum numbers of this boson are consistent with those predicted by the Standard Model (SM) (Chatrchyan et al. 2013; Aad et al. 2013), and that the relative branching ratios (BRs) to SM particles are similarly well described. With this in mind, a window of opportunity now opens for the search for new bosons.

In this paper we will be exploring the possibility of a two-Higgs doublet model with an additional singlet scalar S (2HDM+ S) providing a Dark Matter (DM) candidate. One of the previously studied implications of a 2HDM+ S model is the production of multiple-leptons through the decay chain $H \rightarrow Sh, SS$ (von Buddenbrock et al. 2016), where H is the heavy CP-even scalar and h is considered as the SM Higgs boson with mass $m_h = 125$ GeV. Excesses in multi-lepton final states were reported in von Buddenbrock et al. (2018). In order to further explore results with more data and new final states, while avoiding biases and look-elsewhere effects, the parameters of the model were fixed in 2017 according to von Buddenbrock et al. (2016, 2018). This includes setting the scalar masses as $m_H = 270$ GeV, $m_S = 150$ GeV, treating S as a SM Higgs-like scalar and assuming the dominance

of the decays $H \rightarrow Sh, SS$. Statistically compelling excesses in opposite sign di-leptons, same-sign di-leptons, and three leptons, with and without the presence of b -tagged hadronic jets were reported in Buddenbrock et al. (2019a); von Buddenbrock et al. (2020); Hernandez et al. (2021). Subsequently, with independent data sets and the phase-space fixed by the above mentioned model, an 8σ combined excess was reported in Buddenbrock et al. (2019b), indicating a statistical preference for 2HDM+ S over the SM alone. These excesses have continued to grow (Hernandez et al. 2021; von Buddenbrock et al. 2020; Crivellin et al. 2021; Fischer et al. 2022). With the procedure followed, the look-elsewhere or trials factors are nullified. In addition, a candidate of S with a mass of 151.5 GeV and a significance of 4.8σ has just been reported in Crivellin et al. (2021). The possible connection with the anomalous magnetic moment of the muon $g-2$ was reported in Sabatta et al. (2020). For a review of various anomalies see Fischer et al. (2022).

Interestingly, the aforementioned 2HDM+ S models can accommodate a DM candidate particle, whose production would contribute to “missing energy” in LHC measurements. As yet, the properties of this particle are not constrained by any of the data from the LHC used in (von Buddenbrock et al. 2016, 2018; Buddenbrock et al. 2019a; von Buddenbrock et al. 2020; Hernandez et al. 2021). This can be utilised to further test the 2HDM+ S model in the context of astrophysical measurements, which indicate that baryonic matter comprises 5% of the current energy density in the universe while DM makes up more than 24% (Aghanim et al. 2020; Koopmans & Treu 2003; Metcalf et al. 2004; Hoekstra et al. 2002; Moustakas &

* Email: geoffrey.beck@wits.ac.za

Metcalf 2003). Thus, the DM candidate of the model could be expected to be probed by observations of regions with high DM density.

In this study we aim to use astrophysics as an indirect probe of the unconstrained elements of the 2HDM+ S model that is, so far, motivated by LHC anomalies. This is done via a DM particle coupling to S as a mediator to the SM, where the non-DM parameters of the collider model are fixed to describe the LHC data (von Buddenbrock et al. 2016, 2019). Since the DM candidate is unconstrained at the LHC, additional observational probes are needed to supplement the collider data. Thus, we will study the potential DM candidate parameter space while holding the other 2HDM+ S parameters fixed. We make particular use of the observed positron excess by the Alpha Magnetic Spectrometer (AMS-02) (Aguilar et al. 2019), anti-protons from the same detector (Aguilar et al. 2016), and the excess in gamma-ray fluxes from the galactic centre measured by Fermi-LAT (Ackermann et al. 2017). This is partially motivated by the fact that the LHC anomalies triggering the 2HDM+ S model are leptonic in nature. These particular astrophysical data sets are of interest as they have been extensively studied as potential signatures of DM (Cholis et al. 2019; Das et al. 2020; Ishiwata et al. 2020; Farzan & Rajaei 2019; Profumo et al. 2020; Li 2018; Giesen et al. 2015; Beck 2019; Beck & Colafrancesco 2016). This DM model is then used to make predictions for radio observations with the MeerKAT precursor to the Square Kilometre Array (SKA). These emissions would result from synchrotron radiation from electrons and positrons produced in DM annihilations. As such, we compute the number of e^+ and p^- as a result of DM annihilations using the model described here from the collider physics perspective, and with the input from the astrophysics, we extend this by ensuring consistency with astrophysical observations. With a constrained DM model, our predictions can then be tested independently via observations with the MeerKAT telescope. In this regard, the complementarity between collider and astroparticle physics is investigated in the model considered here. Furthermore, the favoured DM candidate mass regions, resulting from astrophysical limits, can be used to motivate collider searches to better probe the properties of the 2HDM+ S model.

This paper is structured as follows. The particle and astroparticle physics models are described in Sections 2 and 3, respectively. Then, Section 4 succinctly describes the MeerKAT telescope. The methodology used here is detailed in Section 5. Results and conclusions are presented in Sections 6 and 7 respectively.

2 PARTICLE PHYSICS MODEL

Here, we succinctly describe the model used to describe the multi-lepton anomalies observed in the LHC data and with which to interpret the above mentioned excesses in astrophysics. The formalism is comprised of a model of fundamental interactions interfaced with a model of cosmic-ray fluxes that emerge from DM annihilation. The potential for a two Higgs-doublet model with an additional real singlet field Φ_S

(2HDM+ S) is given as in von Buddenbrock et al. (2016):

$$\begin{aligned} V(\Phi) = & m_{11}^2 |\Phi_1|^2 + m_{22}^2 |\Phi_2|^2 - m_{12}^2 (\Phi_1^\dagger \Phi_2 + \text{h.c.}) \\ & + \frac{\lambda_1}{2} (\Phi_1^\dagger \Phi_1)^2 + \frac{\lambda_2}{2} (\Phi_2^\dagger \Phi_2)^2 + \lambda_3 (\Phi_1^\dagger \Phi_1) (\Phi_2^\dagger \Phi_2) \\ & + \lambda_4 (\Phi_1^\dagger \Phi_2) (\Phi_2^\dagger \Phi_1) + \frac{\lambda_5}{2} [(\Phi_1^\dagger \Phi_2)^2 + \text{h.c.}] \\ & + \frac{1}{2} m_S^2 \Phi_S^2 + \frac{\lambda_6}{8} \Phi_S^4 + \frac{\lambda_7}{2} (\Phi_1^\dagger \Phi_1) \Phi_S^2 \\ & + \frac{\lambda_8}{2} (\Phi_2^\dagger \Phi_2) \Phi_S^2. \end{aligned} \quad (1)$$

The fields Φ_1 , Φ_2 in the potential are the $SU(2)_L$ Higgs doublets. The first three lines in Eq. (1) are the contributions of the real 2HDM potential. The terms of the last line are contributions of the singlet field Φ_S . To prevent the tree-level flavour changing neutral currents we consider a \mathbb{Z}_2 symmetry which can be softly broken by the term $m_{12}^2 \neq 0$. After the minimisation of the potential and electro-weak symmetry breaking, the scalar sector is populated with three CP even scalars h (SM Higgs), H and S , one CP odd scalar A and charged scalar H^\pm . For more details of this model and associated interactions' Lagrangians and parameter space we refer to von Buddenbrock et al. (2016, 2019). Further, we consider interactions of S with three types of DM candidate (χ). These will correspond to the possibility of χ having either spin 0, 1/2, or 1. The interactions take the forms:

$$\mathcal{L}_{\text{int},0} = \frac{1}{2} m_\chi g_\chi^S \chi \chi S, \quad (2)$$

$$\mathcal{L}_{\text{int},1/2} = \bar{\chi} (g_\chi^S + i g_\chi^P \gamma_5) \chi S, \quad (3)$$

$$\mathcal{L}_{\text{int},1} = g_\chi^S \chi^\mu \chi_\mu S, \quad (4)$$

where g_χ^S is the strength of the scalar coupling between DM and the singlet real scalar S , g_χ^P is the strength of the pseudo-scalar coupling to S , and m_χ is the DM mass. Having these interactions in mind, we consider the processes $\chi \bar{\chi} \rightarrow S \rightarrow X$ and $\chi \bar{\chi} \rightarrow S \rightarrow H S/h \rightarrow X$ (where X represents some Standard Model products). We will term these 2 \rightarrow 2 and 2 \rightarrow 3 for brevity. The motivation for this pair of interactions is that they are the simplest options available.

It is important to note that the non-DM model parameters for the 2HDM+ S model are fixed according to von Buddenbrock et al. (2016, 2018). Some of the most relevant values here being that $m_S = 150$ GeV and $m_H = 270$ GeV. Since the S boson is assumed to have Higgs-like branching ratios to the SM, the mass of these particles will directly effect the $\chi \chi \rightarrow$ SM products, as the SM branching ratios scale with m_S .

Finally, the DM candidate degree of freedom is, as yet, unconstrained by LHC data. Therefore, we will scan a wide parameter space, from the lowest DM masses that can produce real S bosons up to 1 TeV. In the 2 \rightarrow 3 case, the lower mass limit is that required to produce H and h bosons together. In this regard, astrophysical searches will compliment LHC data by probing aspects of the 2HDM+ S model that are not yet determined by collider data.

3 ASTROPHYSICAL MODELLING

Here we will discuss the models used to determine both cosmic-ray and photon fluxes arriving at Earth as a result of

DM annihilation. Considering the source halos as the Milky Way (cosmic rays) and Reticulum II (photons).

The principle equation of interest, in this regard, will be the diffusion-loss equation for a particle species i :

$$\frac{\partial}{\partial t} \frac{dn_i}{dE} = \vec{\nabla} \cdot \left(D(E, \vec{x}) \vec{\nabla} \frac{dn_i}{dE} \right) + \frac{\partial}{\partial E} \left[b(E, \vec{x}) \frac{dn_i}{dE} \right] + Q_i(E, \vec{x}), \quad (5)$$

where D is the diffusion function, b is the energy-loss function, Q_i is the source function for i -particles, and $\frac{dn_i}{dE} = \frac{dn_i}{dE}(E, \vec{x})$ is the number density per unit energy of i -particles. In particular, the equilibrium solutions of Eq. (5) will provide the distributions of particles injected by DM annihilations within a given astrophysical environment.

In all considered scenarios we will require a source function. This represents the rate of injection of DM annihilation products i , with energy E , into the halo at position \vec{x} . It is given by

$$Q_i = \frac{1}{2} \left(\frac{\rho_\chi(\vec{x})}{m_\chi} \right)^2 \langle \sigma V \rangle \frac{dn_i}{dE} \Big|_{\text{inj}}, \quad (6)$$

where $\frac{dn_i}{dE} \Big|_{\text{inj}}$ is the injected number density of i -particles per unit energy, $\rho_\chi(\vec{x})$ is the DM density at \vec{x} , and $\langle \sigma V \rangle$ is the velocity averaged annihilation cross-section for DM particles.

3.1 Cosmic rays fluxes

Here we will outline the method for calculating the fluxes of positrons and anti-protons that arrive at Earth as a result of DM annihilation within the Milky Way galactic centre. To compute these fluxes we will rely upon equilibrium solutions $\frac{dn_i}{dE}$ to Eq. (5) taken from Cirelli et al. (2011). In doing so we note that the function $D(E, \vec{x})$ depends upon assumptions about the Milky-Way diffusion environment (Maurin et al. 2001) and we explore all three value sets MIN, MED, and MAX presented in Cirelli et al. (2011).

For positrons, these equilibrium solutions yield the flux in the solar neighbourhood via:

$$\frac{d\Phi_{e^+}}{dE} = \frac{c \langle \sigma V \rangle}{8\pi b(E)} \left(\frac{\rho_\odot}{m_\chi} \right)^2 \int_E^{m_\chi} dE_s \frac{dn_{e^+}}{dE_s} \Big|_{\text{inj}} I_\odot(E, E_s), \quad (7)$$

where E_s is the energy of injected positrons, and $I_\odot(E, E_s)$ is a Green's function solving Eq. (5) at the location of Earth, this being given by Cirelli et al. (2011).

Similarly, the anti-proton flux in the solar neighbourhood can be determined, according to Cirelli et al. (2011), as being given by:

$$\frac{d\Phi_{\bar{p}}}{dK} = \frac{v_{\bar{p}}}{8\pi} \langle \sigma V \rangle \left(\frac{\rho_\odot}{m_\chi} \right)^2 R(K) \langle \sigma V \rangle \frac{dn_{\bar{p}}}{dK} \Big|_{\text{inj}}, \quad (8)$$

where K is anti-proton kinetic energy, $v_{\bar{p}}$ is the anti-proton speed, $R(K)$ are the propagation functions from Cirelli et al. (2011), and $\frac{dn_{\bar{p}}}{dK} \Big|_{\text{inj}}$ is the injected anti-proton spectrum.

3.2 Photon fluxes

This section will be concerned with photons produced within the environment of the Reticulum II dwarf galaxy. These include primary photons, produced in the annihilation of DM,

and secondary photons that result from the interaction of annihilation products (electrons and positrons) with their environment. These latter mechanisms will be inverse-Compton scattering of CMB photons, bremsstrahlung with ambient ions, and synchrotron radiation due to the magnetic field within Reticulum II itself.

3.2.1 Primary fluxes

Primary photon fluxes within radius r of a halo centre, at frequency ν are found via:

$$S_\gamma(\nu, r) = \int_0^r d^3r' \frac{Q_\gamma(\nu, r')}{4\pi(d_L^2 + (r')^2)}, \quad (9)$$

where Q_γ is the photon source function and where d_L is the luminosity distance to the halo centre. The integral in Eq. (9) will be taken over some chosen region of interest in each studied target.

3.2.2 Secondary fluxes

Secondary photon fluxes (from electrons produced by DM annihilation) are found using the emissivity:

$$j_i(\nu, r) = \int_0^{m_\chi} dE \frac{dn_{e^\pm}}{dE}(E, r) P_i(\nu, E, r), \quad (10)$$

where $\frac{dn_{e^\pm}}{dE}$ is the sum of the electron and positron distributions (equilibrium solutions to Eq. (5)) within the source region and P_i is the power emitted at frequency ν through mechanism i by an electron with energy E , at position r . The P_i functions are detailed later. The flux produced within a radius r is then found via:

$$S_i(\nu, r) = \int_0^r d^3r' \frac{j_i(\nu, r')}{4\pi(d_L^2 + (r')^2)}. \quad (11)$$

As the environment we consider is one of a dwarf galaxy we must take diffusion into account when solving Eq. (5) (Baltz & Wai 2004) to determine $\frac{dn_{e^\pm}}{dE}$. For all secondary fluxes we solve Eq. (5) with a Green's function method. Assuming spherical symmetry, we have that (Baltz & Edsjö 1998; Baltz & Wai 2004; Colafrancesco et al. 2006, 2007):

$$\frac{dn_e}{dE}(r, E) = \frac{1}{b(E)} \int_E^{m_\chi} dE' G(r, E, E') Q_e(r, E'), \quad (12)$$

this solution method requires that b and D have no spatial dependency, thus they are defined

$$D(E) = D_0 \left(\frac{d_0}{1 \text{ kpc}} \right)^{\frac{2}{3}} \left(\frac{\bar{B}}{1 \mu\text{G}} \right)^{-\frac{1}{3}} \left(\frac{E}{1 \text{ GeV}} \right)^{\frac{1}{3}}, \quad (13)$$

where $D_0 = 3.1 \times 10^{28} \text{ cm}^2 \text{ s}^{-1}$ (Regis et al. 2014), d_0 is the magnetic field coherence length, \bar{B} is the average magnetic field strength, and E is the electron energy. The loss-function is found via (Colafrancesco et al. 2006; Egorov & Pierpaoli 2013):

$$\begin{aligned} b(E) = & b_{\text{IC}} \left(\frac{E}{1 \text{ GeV}} \right)^2 + b_{\text{sync}} \left(\frac{E}{1 \text{ GeV}} \right)^2 \left(\frac{\bar{B}}{1 \mu\text{G}} \right)^2 \\ & + b_{\text{Coul}} \left(\frac{\bar{n}}{1 \text{ cm}^{-3}} \right) \left(1 + \frac{1}{75} \log \left(\frac{\gamma}{1 \text{ cm}^{-3}} \right) \right) \\ & + b_{\text{brem}} \left(\frac{\bar{n}}{1 \text{ cm}^{-3}} \right) \left(\frac{E}{1 \text{ GeV}} \right), \end{aligned} \quad (14)$$

where \bar{n} is the average gas density, the coefficients b_{IC} , b_{sync} , b_{Coul} , b_{brem} are the energy-loss rates from ICS, synchrotron emission, Coulomb scattering, and bremsstrahlung. These coefficients are given by $0.25 \times 10^{-16} (1+z)^4$ (for CMB target photons), 0.0254×10^{-16} , 6.13×10^{-16} , 4.7×10^{-16} in units of GeV s^{-1} . The average quantities \bar{n} and \bar{B} are computed by weighting the average with ρ_χ^2 , ensuring they accurately reflect the environment of the majority of annihilations.

The Green's function is then given by:

$$G(r, E, E') = \frac{1}{\sqrt{4\pi\Delta v}} \sum_{n=-\infty}^{\infty} (-1)^n \int_0^{r_{\text{max}}} dr' \frac{r'}{r_n} f_{G,n}(r, r', \Delta v), \quad (15)$$

$$f_{G,n}(r, r', \Delta v) = \left(e^{-\left(\frac{r'-r_n}{4\Delta v}\right)^2} - e^{-\left(\frac{r'+r_n}{4\Delta v}\right)^2} \right) \frac{Q_e(r')}{Q_e(r)}, \quad (16)$$

with the sum running over a set of image charges, each at position $r_n = (-1)^n r + 2nr_{\text{max}}$, where $r_{\text{max}} = 2r_{\text{vir}}$ or twice the virial radius. The additional required definitions have:

$$\Delta v = v(u(E)) - v(u(E')), \quad (17)$$

with

$$\begin{aligned} v(u(E)) &= \int_{u_{\text{min}}}^{u(E)} dx D(x), \\ u(E) &= \int_E^{E_{\text{max}}} \frac{dx}{b(x)}, \end{aligned} \quad (18)$$

where $E_{\text{max}} = m_\chi$.

3.2.3 Secondary emission power functions

In this section we will detail the power functions P_i for synchrotron, inverse-Compton, and bremsstrahlung emission.

For synchrotron emission we have that an electron of energy E , at position r radiates power at frequency ν given by (Longair 1994; Rybicki & Lightman 1986):

$$P_{\text{sync}}(\nu, E, r) = \int_0^\pi d\theta \frac{\sin \theta^2}{2} 2\pi\sqrt{3}r_e m_e c \nu_g F_{\text{sync}} \left(\frac{\kappa}{\sin \theta} \right), \quad (19)$$

where ν_g is the non-relativistic gyro-frequency, r_e is the electron radius, m_e is the electron mass, and θ is the angle between the magnetic field and electron trajectory. The value of κ is found via:

$$\kappa = \frac{2\nu}{3\nu_g \gamma^2} \left[1 + \left(\frac{\gamma \nu_p}{\nu} \right)^2 \right]^{\frac{3}{2}}, \quad (20)$$

with $\gamma = \frac{E}{m_e c^2}$. Finally,

$$F_{\text{sync}}(x) \simeq 1.25 x^{\frac{1}{3}} e^{-x} (648 + x^2)^{\frac{1}{12}}. \quad (21)$$

The power produced by the inverse-Compton scattering (ICS) at a photon of frequency ν from an electron with energy E is given by Longair (1994); Rybicki & Lightman (1986):

$$P_{\text{IC}}(\nu, E) = cE_\gamma(z) \int d\epsilon n(\epsilon) \sigma(E, \epsilon, E_\gamma), \quad (22)$$

where ϵ is the energy of the seed photons distributed according to $n(\epsilon)$ (this will taken to be that of the CMB), and

$$\sigma(E, \epsilon, E_\gamma) = \frac{3\sigma_T}{4\epsilon\gamma^2} G(q, \Gamma_e), \quad (23)$$

with σ_T being the Thompson cross-section and

$$G(q, \Gamma_e) = 2q \ln q + (1+2q)(1-q) + \frac{(\Gamma_e q)^2 (1-q)}{2(1+\Gamma_e q)}, \quad (24)$$

with

$$q = \frac{E_\gamma}{\Gamma_e (\gamma m_e c^2 + E_\gamma)}, \quad \Gamma_e = \frac{4\epsilon\gamma}{m_e c^2}, \quad (25)$$

where m_e is the electron mass.

Finally, the power from bremsstrahlung at photon energy E_γ from an electron at energy E is given by (Longair 1994; Rybicki & Lightman 1986):

$$P_{\text{brem}}(E_\gamma, E, r) = cE_\gamma \sum_j n_j(r) \sigma_B(E_\gamma, E), \quad (26)$$

where n_j is the distribution of target nuclei of species j and the cross-section is given by:

$$\sigma_B(E_\gamma, E) = \frac{3\alpha\sigma_T}{8\pi E_\gamma} \left[\left(1 + \left(1 - \frac{E_\gamma}{E} \right)^2 \right) \phi_1 - \frac{2}{3} \left(1 - \frac{E_\gamma}{E} \right) \phi_2 \right], \quad (27)$$

with ϕ_1 and ϕ_2 being energy dependent factors determined by the species j (see Longair (1994); Rybicki & Lightman (1986)).

4 MEERKAT AND THE SKA

Indirect detection of DM has been traditionally focused upon the use of gamma-ray experiments, such as the Fermi-LAT (Atwood et al. 2009), because this mode of detection has low attenuation in the interstellar medium and has high detection efficiency. Recently, the indirect hunt for DM in radio-band has become prominent. This emerges from the fact that radio interferometers have an angular resolution vastly transcending that of gamma-ray experiments. Of particular interest to this work is the SKA, an international science project designed for studies in the field of radio astronomy. This telescope array provides around 50 times the sensitivity and 10,000 times the survey speed of the best current telescopes (Dewdney et al. 2012). These capabilities have already been extensively argued to provide a powerful tool for exploring the properties of DM via indirect detection of annihilation or decay products (Colafrancesco et al. 2015; Beck & Colafrancesco 2016; Beck 2019). At present, the precursor array MeerKAT is currently being operated by the South African Radio Astronomy Observatory (SARAO) with 64 antennae elements. Each of the elements is a 13.5 m diameter dish, configured to achieve high sensitivity and wide field-of-view imaging of the sky. With 20 hours of time on target it is estimated that MeerKAT can achieve an rms sensitivity of $2.45 \mu\text{Jy beam}^{-1}$ at robust weighting 0, this is sourced from SARAO's publicly available tools¹. This results in sensitivity, at arcminute scales, of $= 2.45 \mu\text{Jy beam}^{-1} \times \left(\frac{1 \text{ arcminute}}{11 \text{ arcseconds beam}^{-1}} \right)^2 \approx 73 \mu\text{Jy}$, when taking into account the synthesized beam size of ≈ 11 arcseconds and assuming arcminute scale emissions. We note that a more tailored estimate of MeerKAT sensitivity, making use of an arcminute-scale taper on the visibilities, will

¹ https://archive-gw-1.kat.ac.za/public/tools/continuum_sensitivity_calculator.html

likely yield an improved sensitivity. This is because the DM emission is diffuse and will be on a scale of arcminutes (Regis et al. 2017), while the visibility taper reduces contributions from long array baselines (Marr et al. 2015), corresponding to small angular scales, which would be dominated by the signal from point-sources. Therefore, $73 \mu\text{Jy}$ therefore constitutes a conservative estimate for arcminute scale sensitivity to diffuse emission. Note that the impact of the taper would be somewhat reduced by the additional need for the subtraction of non-DM emission sources.

The sensitivity of MeerKAT is around a factor of 2 better than ATCA² which has previously been used for indirect DM searches in dwarf galaxies (Regis et al. 2017). This notable sensitivity advantage is a consequence of the instrument exceeding its original design specifications, see Booth et al. (2009); Dewdney et al. (2012), making it an unexpected new leader in radio-frequency DM searches. Additionally, MeerKAT is expected to receive an upgrade of an additional 20 dishes, taking it to 84, with construction expected to be complete in 2023.³

When computing SKA sensitivities we make use of Tables 6 and 7 from Braun et al. (2019) we perform a similar scaling to get $\mu\text{Jy arcmin}^{-2}$ as with MeerKAT, but we use the geometric mean of quoted minimum and maximum beam sizes. This will likely result in conservative estimates for the sensitivity.

5 METHODOLOGY

The methodology we follow is that we generate the per-annihilation yield functions $\frac{dn_i}{dE}$ for positrons, anti-protons, and photons via Monte Carlo (MC) event generators. We then use these as ingredients for our models from Section 3. The model results are compared to data from cosmic-ray and gamma-ray excesses to find a best-fit parameter space, in terms of m_χ and $\langle\sigma V\rangle$. Finally, this is used to produce predictions for observable radio emissions and non-observation limits with MeerKAT and the SKA. Each of these steps is detailed below.

5.1 Annihilation yield functions

We use an MC generator to simulate the production of particles as a result of the annihilation of DM through S according to the model described in Section 2. We make use of MG5_@MC (Alwall et al. 2011) as our primary tool to generate events for the $2 \rightarrow 2$ and $2 \rightarrow 3$ scattering processes. The MC generator is interfaced with Pythia 8 (Sjöstrand et al. 2008) to hadronize intermediate partons. We varied the DM mass between 200 to 1000 GeV for the $2 \rightarrow 3$ scattering and 75 to 1000 GeV for the $2 \rightarrow 2$ scattering with 100 GeV spacing. In Fig. 1 and 2 we display a complete set of yield spectra for positrons and anti-protons for $2 \rightarrow 2$ and $2 \rightarrow 3$ scattering. These graphs display the number of particles per annihilation per unit energy, $\frac{dn_i}{dE}$, and the yield functions binned in energy intervals of 0.5 GeV. Results are displayed for spin-0

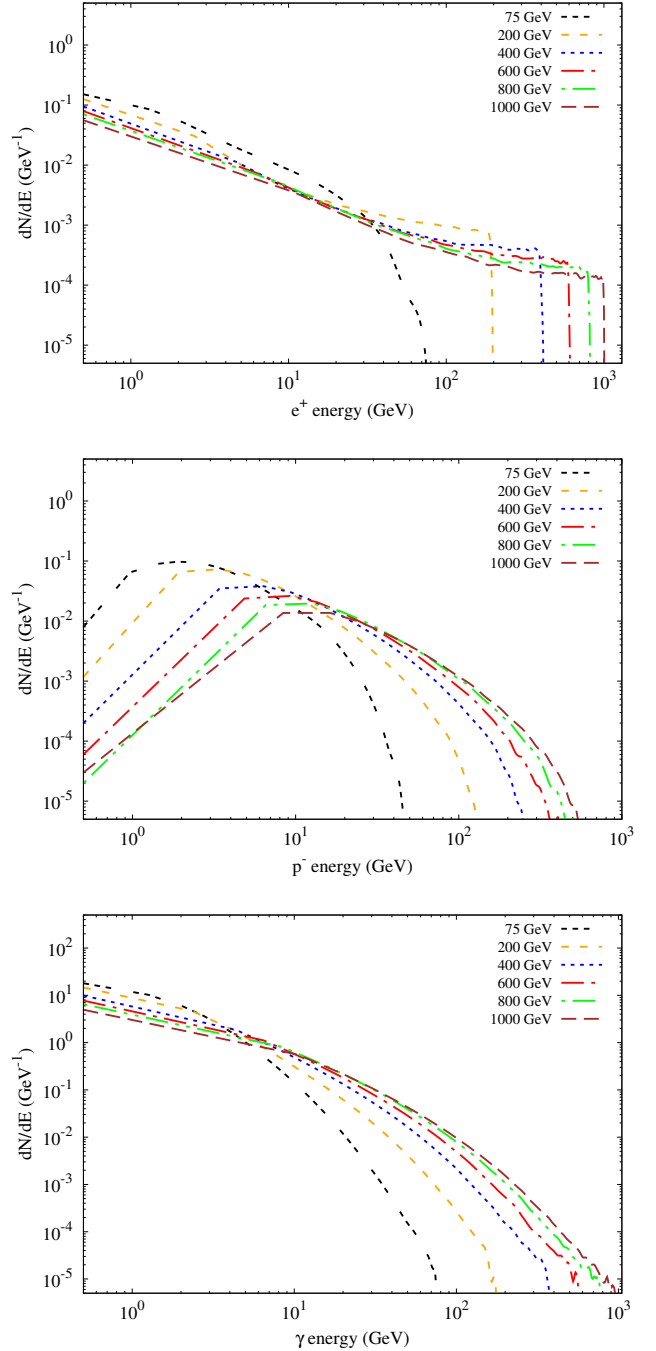


Figure 1. Differential yields of positrons, anti-protons and photons for the $2 \rightarrow 2$ annihilation process of Spin-0 DM for a variety of WIMP masses. Model parameters are fixed according to von Buddenbrock et al. (2016, 2018), based on LHC data.

DM. A notable result is that the yield functions per annihilation are not significantly different for the other spin choices. However, the cross-section for the $2 \rightarrow 3$ process is several orders of magnitude smaller than that of the $2 \rightarrow 2$ case. We will thus prioritise this latter scenario in our presented

² https://www.narrabri.atnf.csiro.au/myatca/interactive_senscalc.html

³ <https://www.mpg.de/15382572/top-radio-telescope-in-south-africa/results>.

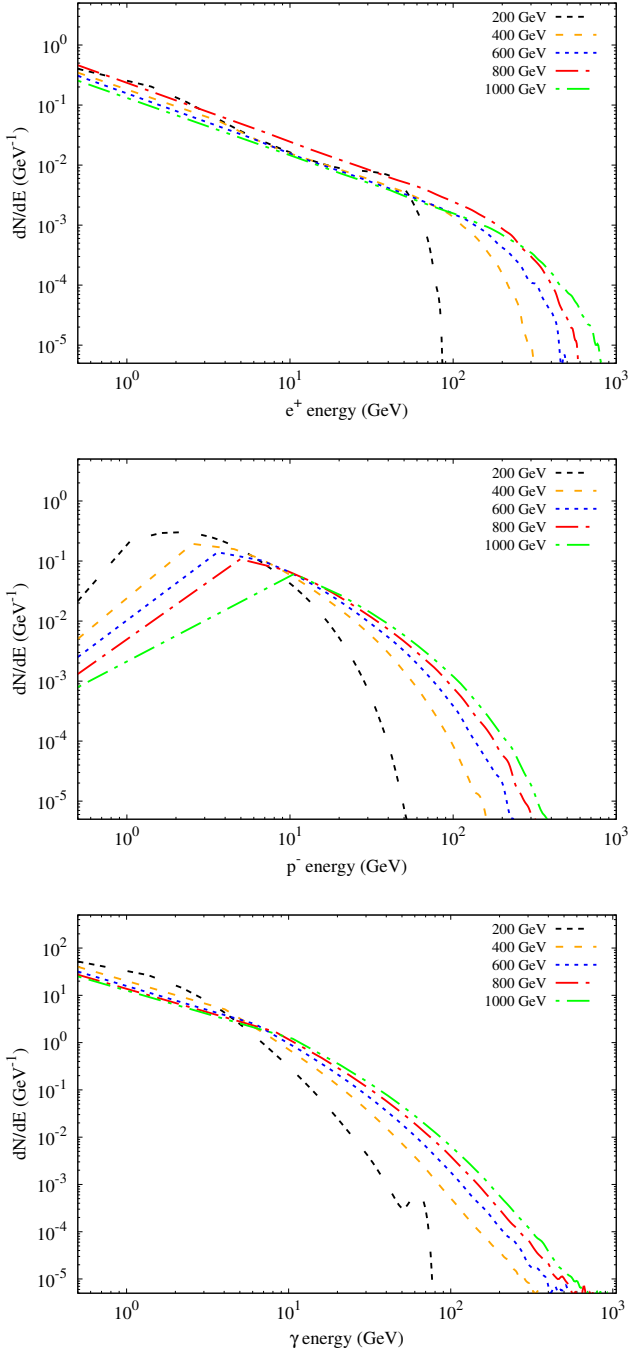


Figure 2. Differential yields of positrons, anti-protons and photons for the $2 \rightarrow 3$ annihilation process of Spin-0 DM for a variety of WIMP masses. Model parameters are fixed according to von Buddenbrock et al. (2016, 2018), based on LHC data.

5.2 Fitting to astrophysical excesses

The annihilation yields, found above, are then used as inputs for indirect DM detection following Eqs. (7) and (8) in the case of the anti-proton and positron fluxes at Earth, and Eqs. (9) and (11) for gamma-rays produced via primary and secondary mechanisms. We will then use cosmic-ray and gamma-ray excess data to determine the region of the DM

parameter space (in terms of m_χ and $\langle\sigma V\rangle$) that best fits to these excesses. The predicted spectra for cosmic-ray fluxes at Earth are compared to data from AMS-02 (Aguilar et al. 2019, 2016). In the case of the anti-protons we use the background model found in Heisig et al. (2020), while for positrons we use a nearby pulsar model for the high-energy background from Fang et al. (2019) (note that this means the DM component is sub-dominant). When we model gamma-ray fluxes from the galactic centre we use fiducial model data from Ackermann et al. (2017), making use of the excess spectrum for a 10° region of interest around the galactic centre. In all cases our Milky-Way halo models follow those presented in Cirelli et al. (2011).

We note that both AMS-02 anomalies have been widely studied, either as constraints on DM models or as potential signatures thereof (Cholis et al. 2019; Das et al. 2020; Ishiwata et al. 2020; Farzan & Rajaei 2019; Profumo et al. 2020; Li 2018; Giesen et al. 2015). The anti-proton case has been argued to be highly significant and most in agreement with the annihilation via b -quarks of a 40 – 70 GeV WIMP with some potential for heavier masses (Cholis et al. 2019). However, an accounting for possibility of correlated errors (Heisig et al. 2020) reveals no preference for a DM contribution from WIMPs between 10 and 1000 GeV in mass. It is also difficult to reconcile such models with existing radio data (Beck 2019). In the case of positrons there is a stark but unexplained excess of positrons at around a few hundred GeV that can potentially be described in terms of DM models and has great potential to be used as a probe of DM physics even with astrophysical backgrounds (Mauro et al. 2016). Additionally, we note that the significance of the widely studied Fermi-LAT galactic centre gamma-ray excess is highly uncertain due to systematics (Ackermann et al. 2017). Notably, Di Mauro (2021) has recently argued that the galactic centre excess remains compatible with a contracted NFW (Navarro et al. 1996) profile (see also the review in Fischer et al. (2022)).

5.3 Multi-frequency emission prediction

Our final step is to use the emission models from section 3.2 to produce multi-frequency spectra for Reticulum II, with a focus on the radio and gamma-ray frequency bands. This we do using Eqs. (9) and (11) and by solving Eq. (5) following the methods detailed in section 3.2. Once these predictions are produced for $\langle\sigma V\rangle$ values sourced from the excess best-fits, we compare them to the sensitivities of MeerKAT and the SKA, following the descriptions in section 4, in order to determine the observability of models in the excess best-fits regions. We also determine non-observation constraints at 95% confidence interval via the same sensitivity estimates.

6 RESULTS

We will display only results for spin 0, as $\langle\sigma V\rangle$ results here are very similar, with only a factor of two difference if the spin 1/2 case is a Dirac fermion. This is due to the yield functions per annihilation $\frac{dn_i}{dE}$ being similar for all spin cases considered. The difference between the different spins occurs largely in the cross-section σ itself. Thus, the choice of spin will largely impact limits on the coupling between DM and S , g_χ^S . Note that we will prioritise the presentation of the $2 \rightarrow 2$

scenario, due to its larger cross-section and better description of the astrophysical data.

In Fig. 3 we display the best-fit parameter space for $2 \rightarrow 2$ scattering with the AMS-02 positron data from Aguilar et al. (2019) and the over-lap regions with the anti-proton and Fermi-LAT galactic centre gamma-ray parameter spaces. In order to account for uncertainties in the modelling of Milky-way DM halo we display the thermal relic cross-section (Steigman et al. 2012) as a band, in order to represent the fact that models within this band are compatible with the relic value up to systematic uncertainties. The uncertainties are derived entirely from estimates of ρ_\odot (see for instance Weber & de Boer (2010); Benito et al. (2019)). The plots in Fig. 3 show that crucial overlap regions fall slightly above the relic band. The regions for all three excesses do not mutually overlap, although it must be noted that systematic issues with the positron and gamma-ray data (Aguilar et al. 2019; Ackermann et al. 2017) indicate that there may be missing ingredients in the astrophysical modelling. Despite this, the 3 regions cluster close together and converge close to the relic region. The presented figure shows the best-case overlap which requires the MED diffusion scenario and an Einasto (or NFW) halo with the parameters drawn from Cirelli et al. (2011). The fact that the uncontracted Einasto and NFW halos produced a closer agreement means that this overlap does not favour a more speculative contracted halo (as is often necessary for DM modelling of these excesses historically) and is compatible with non-extremal diffusion conditions. This stands in contrast with model independent searches like Di Mauro (2021), where it is argued that a contracted DM profile is favoured for a DM-related explanation of the galactic centre excess spectrum from Ackermann et al. (2017). This difference may be down to the fact that we only make a spectral comparison to the excess, whereas cases like Di Mauro (2021) motivate the halo shape via spatial matching as well. It is notable that, despite our inclusion of a large positron background from a nearby pulsar (Fang et al. 2019), the favoured cross-sections remain large, indicating that DM is still playing a role in reconciling the AMS-02 positron data. We have made some initial verification that the parameter space of the 2HDM+S model that describes LHC and astrophysics data are not excluded by direct DM searches. In particular, for a Type-II 2HDM+S limits become weak when the ratio of the vacuum expectation values of the complex doublets, $\tan \beta < 1$ (Bell et al. 2017), which is preferred by the LHC data (von Buddenbrock et al. 2019). This evasion of direct detection is possible as S acts as a mediator between DM and the SM and is not produced directly from the SM at the LHC (it results from H decays). This allows the direct signal to remain small without affecting the collider or indirect results. However, more in-depth analysis may be needed on this point. The best-fit DM parameter spaces are summarised in Tables 1 and 2.

Next, we will consider the comparison between the sensitivity of the MeerKAT telescope and the predicted emissions for our constrained DM model using the Reticulum II dwarf galaxy. The choice of this target is motivated by the fact that it is in an ideal location for southern hemisphere observations and has one of the highest ‘J-factors’ among known dwarf galaxies (Albert et al. 2017). In fitting with our AMS-02 constraints from Fig. 3, we assume $\langle \sigma V \rangle = 10^{-25} \text{ cm}^3 \text{ s}^{-1}$. Note that we also include a shaded uncertainty band in our plots,

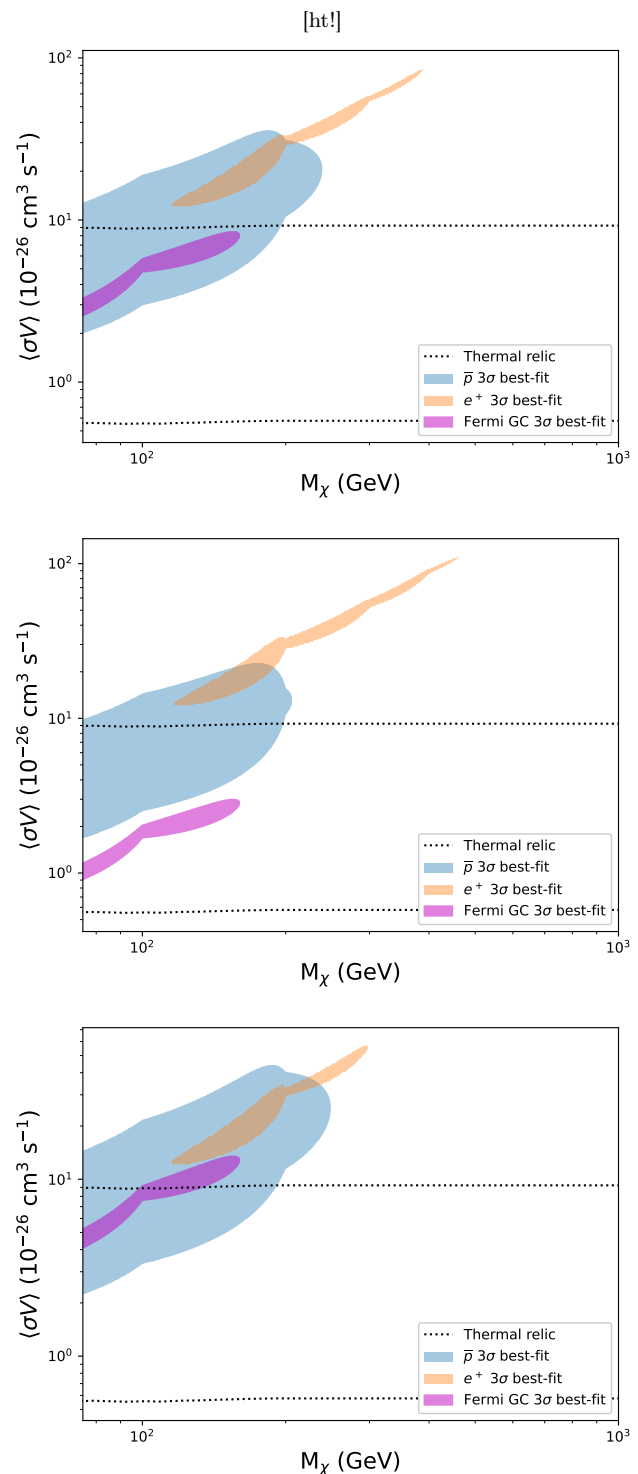


Figure 3. The parameter space fitting the $2 \rightarrow 2$ scattering to the Fermi-LAT galactic centre excess, AMS-02 anti-proton and positron spectra. The shaded regions represent the 3σ confidence interval. The region between the thermal relic lines represents the uncertainties in local DM density and galactic halo profile. This plot assumes the MED diffusion scenario. The 3 plots correspond to different Milky-Way DM halo profiles from Cirelli et al. (2011). *Top:* Einasto profile. *Middle:* contracted Einasto. *Bottom:* NFW.

| | M_χ | Lower | Upper |
|-------|----------|-------|-------|
| | 75.0 | 2.6 | 3.3 |
| | 81.1 | 2.9 | 3.7 |
| | 87.1 | 3.3 | 4.2 |
| | 93.2 | 3.8 | 4.8 |
| | 99.2 | 4.7 | 5.7 |
| | 105.3 | 4.9 | 6.1 |
| [ht!] | 111.3 | 5.0 | 6.4 |
| | 117.4 | 5.1 | 6.7 |
| | 123.5 | 5.3 | 7.1 |
| | 129.5 | 5.5 | 7.4 |
| | 135.6 | 5.7 | 7.7 |
| | 141.6 | 6.1 | 8.0 |
| | 147.7 | 6.4 | 8.3 |
| | 153.8 | 6.9 | 8.4 |
| | 159.8 | 7.8 | 8.2 |

| M_χ | Lower | Upper | M_χ | Lower | Upper |
|----------|-------|-------|----------|-------|-------|
| 115.2 | 12.1 | 12.4 | 75.0 | 2.0 | 12.8 |
| 134.7 | 12.7 | 16.6 | 86.7 | 2.4 | 15.3 |
| 154.2 | 14.4 | 21.3 | 98.4 | 2.9 | 18.5 |
| 173.7 | 17.1 | 27.2 | 110.1 | 3.2 | 20.7 |
| 193.2 | 23.5 | 33.5 | 121.8 | 3.5 | 22.8 |
| 212.8 | 30.0 | 35.3 | 133.5 | 3.8 | 25.2 |
| 232.3 | 32.7 | 40.2 | 145.2 | 4.2 | 28.0 |
| 251.8 | 36.3 | 44.7 | 156.9 | 4.8 | 31.0 |
| 271.3 | 41.2 | 50.7 | 168.6 | 5.5 | 33.8 |
| 290.9 | 48.2 | 56.7 | 180.3 | 6.6 | 35.7 |
| 310.4 | 56.2 | 61.0 | 192.0 | 8.4 | 34.9 |
| 329.9 | 61.0 | 66.9 | 203.7 | 10.9 | 30.9 |
| 349.4 | 66.5 | 72.9 | 215.4 | 12.2 | 29.5 |
| 369.0 | 73.4 | 79.3 | 227.1 | 14.3 | 27.2 |
| 388.5 | 84.3 | 86.3 | 238.8 | 19.7 | 21.2 |

Table 1. The 3σ confidence interval best-fit parameter spaces for the 2HDM+S model as well as the MED scenario, $2 \rightarrow 2$ processes, and an Einasto halo in the Milky-Way. The limits are presented as the upper and lower edges of contour ($10^{-26} \text{ cm}^3 \text{ s}^{-1}$) for each mass (GeV). *Left:* Fermi-LAT GeV gamma-rays. *Centre:* AMS-02 positrons. *Right:* AMS-02 anti-protons.

this includes uncertainties on the value of ρ_\odot , the magnetic field, and the J-factor. We make use of a cored density profile following arguments from Walker et al. (2009); Adams et al. (2014). This being an Einasto profile (Einasto 1968) (which can be cored for certain parameter choices), given by:

$$\rho_e(r) = \rho_s \exp \left[-\frac{2}{\alpha} \left(\left[\frac{r}{r_s} \right]^\alpha - 1 \right) \right], \quad (28)$$

where we follow Regis et al. (2017) in having $\alpha = 0.4$, $r_s = 0.2$ kpc, and $\rho_s = 7 \times 10^7 \text{ M}_\odot \text{ kpc}^{-3}$. We then follow Regis et al. (2017) in using the profiles for gas density and magnetic field strength:

$$n_e(r) = n_0 \exp \left(-\frac{r}{r_d} \right), \quad B(r) = B_0 \exp \left(-\frac{r}{r_d} \right). \quad (29)$$

We take r_d to be given by the stellar-half-light radius with a value of 35 pc (Bechtol et al. 2015; Koposov et al. 2015) and we assume $B_0 \approx 1 \mu\text{G}$, $n_0 \approx 10^{-6} \text{ cm}^{-3}$. The region of flux integration are taken as 3 arcminutes for radio and 30 arcminutes for gamma-rays. The first is in keeping with our assumption of arcminute scale emissions when determining

| | M_χ | Lower | Upper |
|-------|----------|-------|-------|
| | 75.0 | 4.1 | 5.2 |
| | 81.1 | 4.6 | 5.9 |
| | 87.1 | 5.2 | 6.7 |
| | 93.2 | 6.1 | 7.7 |
| | 99.2 | 7.4 | 9.0 |
| | 105.3 | 7.7 | 9.6 |
| [ht!] | 111.3 | 7.9 | 10.2 |
| | 117.4 | 8.2 | 10.7 |
| | 123.5 | 8.4 | 11.2 |
| | 129.5 | 8.8 | 11.8 |
| | 135.6 | 9.2 | 12.3 |
| | 141.6 | 9.6 | 12.8 |
| | 147.7 | 10.2 | 13.2 |
| | 153.8 | 11.0 | 13.5 |
| | 159.8 | 12.5 | 13.1 |

| M_χ | Lower | Upper | M_χ | Lower | Upper |
|----------|-------|-------|----------|-------|-------|
| 115.2 | 12.1 | 12.7 | 75.0 | 2.2 | 14.5 |
| 128.2 | 12.4 | 15.4 | 87.4 | 2.7 | 17.5 |
| 141.2 | 13.3 | 17.9 | 99.8 | 3.3 | 21.6 |
| 154.2 | 14.4 | 21.3 | 112.2 | 3.6 | 24.0 |
| 167.2 | 16.3 | 25.2 | 124.7 | 4.0 | 26.9 |
| 180.2 | 18.9 | 29.9 | 137.1 | 4.4 | 30.2 |
| 193.2 | 23.8 | 33.5 | 149.5 | 5.0 | 33.9 |
| 206.3 | 29.9 | 34.3 | 161.9 | 5.7 | 38.1 |
| 219.3 | 31.6 | 36.7 | 174.3 | 6.7 | 42.1 |
| 232.3 | 33.5 | 40.2 | 186.7 | 8.3 | 44.2 |
| 245.3 | 35.9 | 43.2 | 199.1 | 11.1 | 41.0 |
| 258.3 | 38.5 | 47.0 | 211.5 | 12.6 | 39.4 |
| 271.3 | 42.2 | 50.7 | 224.0 | 14.5 | 37.6 |
| 284.4 | 46.9 | 54.4 | 236.4 | 17.1 | 34.4 |
| 297.4 | 54.4 | 57.0 | 248.8 | 24.4 | 26.1 |

Table 2. The 3σ confidence interval best-fit parameter spaces for the 2HDM+S model as well as the MED scenario, $2 \rightarrow 2$ processes, and an NFW halo in the Milky-Way. The limits are presented as the upper and lower edges of contour ($10^{-26} \text{ cm}^3 \text{ s}^{-1}$) for each mass (GeV). *Left:* Fermi-LAT GeV gamma-rays. *Centre:* AMS-02 positrons. *Right:* AMS-02 anti-protons.

sensitivity. The second is to reflect Fermi-LAT observations from Albert et al. (2017).

Fig. 4 shows that Reticulum II with the Einasto profile produces radio fluxes detectable at 2σ confidence interval with MeerKAT across the mass range (although the $2 \rightarrow 2$ 200 GeV case is very marginal). Only the lower masses are detectable at 5σ . However, the entire uncertainty band is not covered in either case. It should be noted that the $2 \rightarrow 3$ case presents slightly weaker emissions. Importantly, we also display the estimated sensitivity of the full SKA (Braun et al. 2019) which manages to probe the entire uncertainty region for both $2 \rightarrow 2$ and $2 \rightarrow 3$ processes at 5σ confidence interval within 100 hours of observing time.

In Fig. 5 we consider the case of a more realistic observing time of 20 hours with MeerKAT. The most notable result here is that the solid-line model within the uncertainty band ($\rho_\odot = 0.4 \text{ GeV cm}^{-3}$, $B_0 = 1 \mu\text{G}$, $J \approx 2 \times 10^{19} \text{ GeV}^2 \text{ cm}^{-5}$) is still MeerKAT-detectable at both 2 and 5 σ for $m_\chi = 75 \text{ GeV}$ and with substantial uncertainty band coverage at 2σ . This should demonstrate that observations of targets like

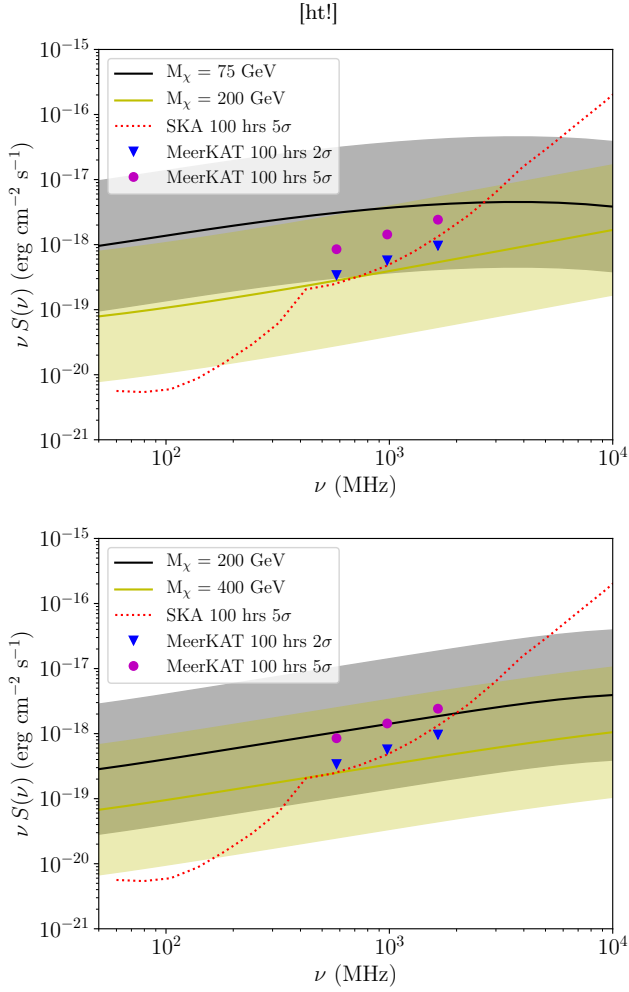


Figure 4. Radio spectrum prediction for Reticulum II with the Einasto profile. The shaded regions encompass the cross-section uncertainties from 3, as well as those from the J-factor of the halo and magnetic field. *Top*: $2 \rightarrow 2$ scattering. *Bottom*: $2 \rightarrow 3$ scattering.

Reticulum II with MeerKAT would prove to be fruitful first steps in probing the 2HDM+S model.

For any MeerKAT 5σ detection prospects across the mass range (i.e. $m_\chi \gtrsim 200$ GeV), at least 1600 hours of observation time would be necessary. Notably this when $B_0 = 1 \mu\text{G}$ and $m_\chi = 200$ GeV. The fact that detection would require such vast lengths of MeerKAT observation time suggests that this is improbable when $B_0 = 1 \mu\text{G}$. However, an increase in sensitivity to $0.5 \mu\text{Jy beam}^{-1}$ would drop the required time to at least 40 hours. Thus, obtaining sub-micro-Jansky sensitivities starts to bring about the practical possibility of detection. This, however, would require the full SKA (Braun et al. 2019). It should be noted that sufficient sensitivity for 2σ exclusion of 2HDM+S model at the fiducial relic cross-section, with the lowest studied DM mass, can be obtained with at least 100 hours on MeerKAT or 6 hours on the sub-micro-Jansky case. The time required to probe a 200 GeV WIMP at the relic level is around one hundred times longer than the 75 GeV case. This is largely due to MeerKAT's limited frequency coverage, which will be ameliorated in the full SKA.

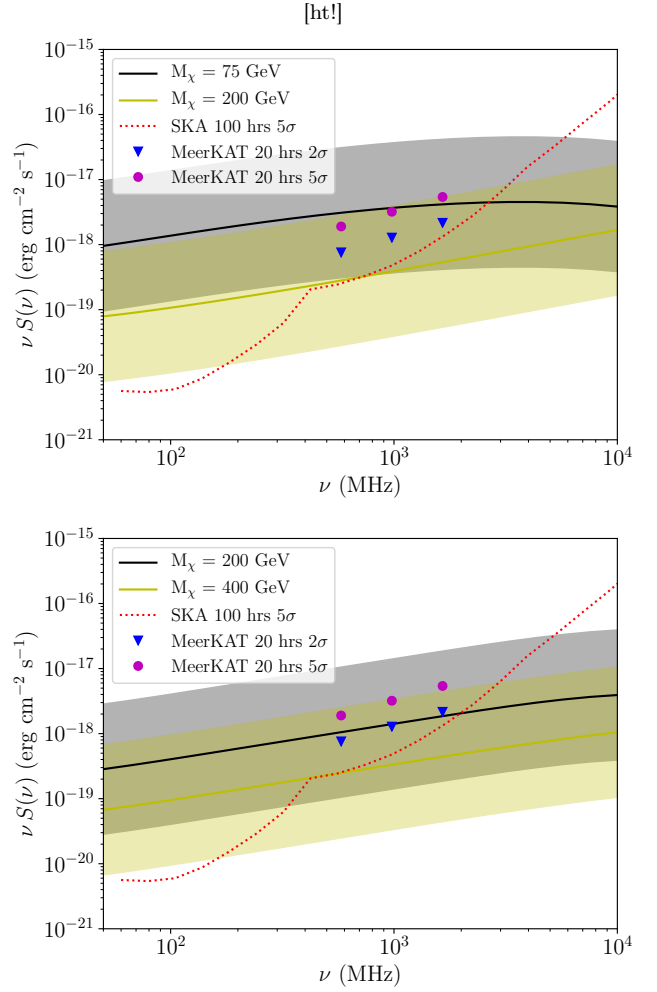


Figure 5. Radio spectrum prediction for Reticulum II with the Einasto profile. The shaded regions encompass the cross-section uncertainties from 3, as well as those from the J-factor of the halo and magnetic field. *Top*: $2 \rightarrow 2$ scattering. *Bottom*: $2 \rightarrow 3$ scattering.

ited frequency coverage, which will be ameliorated in the full SKA.

One point to note is that of the search prospects will likely improve when a visibility taper is considered, as this suppresses the long array baselines, tuning the sensitivity towards larger scale emissions (Marr et al. 2015). This consideration makes the presented results somewhat conservative.

In Fig. 6 we display the potential non-observation constraints from 100 hours of observation of Reticulum II with both MeerKAT and the SKA. MeerKAT can only probe the 2HDM+S model down to the thermal relic cross-section for DM masses $\lesssim 75$ GeV. However, it can exclude a significant part of the excess overlap regions for the astrophysical excesses when $\rho_\odot = 0.4 \text{ GeV cm}^{-3}$, in both cases of NFW and Einasto density profiles for the Milky-Way. The current uncertainties in the local DM density mean the overlap region from Fig. 3 can potentially evade MeerKAT exclusion with 100 hours of observation time if the local density is $\rho_\odot \sim 0.8 \text{ GeV cm}^{-3}$. This is, however, an extreme scenario. Thus, MeerKAT shows considerable potential to probe the

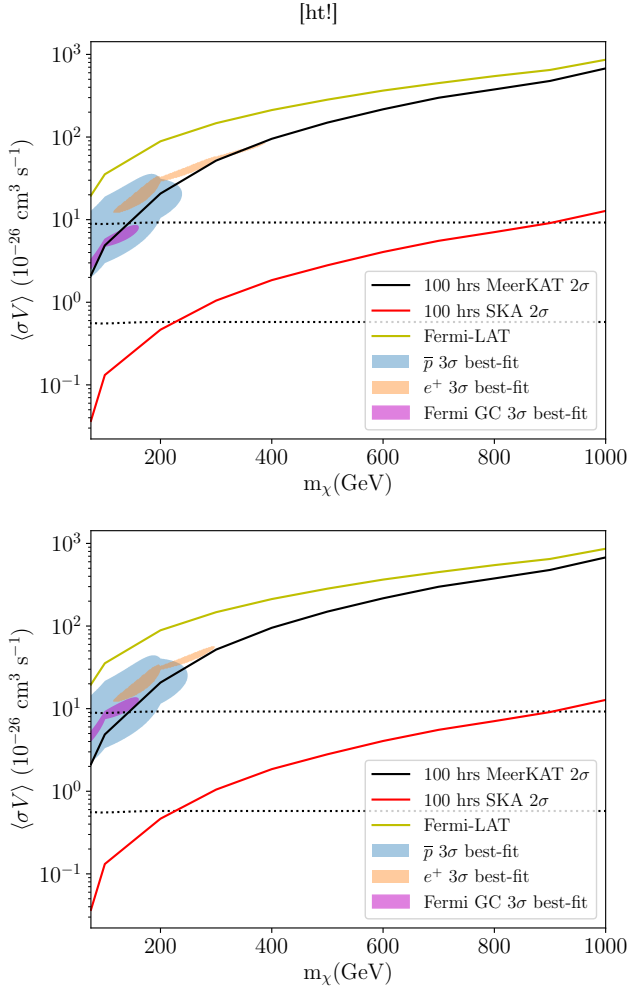


Figure 6. Non-observation 2σ exclusion projections for Reticulum II (Einasto profile) with MeerKAT and the SKA. *Top:* Milkyway-Way galactic centre with Einasto profile. *Bottom:* Milkyway-Way galactic centre with NFW profile. The shaded regions are drawn from Fig. 3. The Fermi-LAT limits are drawn from data found in [Albert et al. \(2017\)](#) and we use a $30'$ integration region in this case.

parameter space corresponding to the 2HDM+ S DM candidate accounting for the studied astrophysical excesses. The potential upper limits are summarised in table 3. Thus, the two-fold sensitivity advantage over previous observations of Reticulum II suggest that even 20 hours on target would yield cutting edge model-independent constraints on channels like b quarks, as [Regis et al. \(2017\)](#) obtained highly competitive non-observation results with 30 hours of ATCA time on this same galaxy.

Next we will translate limits on $\langle\sigma V\rangle$ from fig. 6 to the coupling between S and χ , g_χ^S , this we will do via the definition

$$\langle\sigma V\rangle = \int \sigma_{\chi\chi}(g_\chi^S = 1) \left(g_\chi^S\right)^2 v f(v) dv, \quad (30)$$

where $\sigma_{\chi\chi}(g_\chi^S = 1)$ is the annihilation cross-section when the coupling is unity and $f(v)$ is a Maxwell-Boltzmann distribution with velocity dispersion 4 km s^{-1} to reflect the Reticulum II halo ([Koposov et al. 2015](#)). In figure 7 we display

| M_χ (GeV) | MeerKAT ($10^{-26} \text{ cm}^3 \text{ s}^{-1}$) | SKA ($10^{-26} \text{ cm}^3 \text{ s}^{-1}$) |
|-------------------|---|---|
| 75 | 2.5 | 0.034 |
| 100 | 6.9 | 0.12 |
| 200 | 27 | 0.43 |
| 300 | 66 | 0.98 |
| 400 | 120 | 1.7 |
| 500 | 190 | 2.6 |
| 600 | 270 | 3.8 |
| 700 | 370 | 5.2 |
| 800 | 470 | 6.6 |
| 900 | 590 | 8.4 |
| 1000 | 830 | 12 |

Table 3. Potential non-observation upper limits on $\langle\sigma V\rangle$ for the 2HDM+ S model in the $2 \rightarrow 2$ scenario. This data assumes the MED diffusion scenario and an Einasto halo profile in the Milky-Way.

the limits on the coupling parameter between χ and S that can be inferred from the results of figure 6 in the $2 \rightarrow 2$ case with spin 0. These demonstrate that this parameter space remains difficult to probe, however, for low m_χ we see that the SKA has the potential to probe below $g_\chi^S = 1$ (the $2 \rightarrow 3$ case provides no real limits as the cross-section is around 10^6 times smaller, suggesting it would be subdominant anyway). It is notable that this coupling is unconstrained by current LHC data. Importantly, spin 1/2 yields similar results whereas spin 1 results are less constraining by several orders of magnitude at every mass considered. This is due to the far smaller $\chi\chi \rightarrow S$ cross-section for spin 1 χ .

7 CONCLUSIONS

In this paper we used a 2HDM+ S model, that describes the multi-lepton anomalies at the LHC, to describe the excesses in gamma-ray flux from the galactic centre and the cosmic-ray spectra from AMS-02. This is achieved through DM annihilation via the singlet scalar into particles of the SM. The parameters of the model are fixed to the LHC data, except for the mass of the DM and the size of the coupling to the mediator S (these being, as yet, unconstrained by collider data). The mass of the DM is scanned, where the coupling of the DM to the mediator S is varied, and various diffusion scenarios are considered. A satisfactory description of the gamma-ray flux from the galactic centre and the cosmic-ray spectra from AMS-02 is obtained with the MED diffusion scenario. The best description of the excesses is obtained for DM masses below 200 GeV. Although complete overlap between all the best-fit regions is not achieved, it is notable that there are unresolved systematics in much of the data. Nonetheless, it is still remarkable that such close agreement can be obtained for a model whose particle physics is set by LHC anomalies.

Predictions of the synchrotron spectrum are made with the model in order to assess the detection sensitivity of MeerKAT in a conservative scenario where no visibility taper is considered. We conducted our test on a fiducial best-fit cross-section of $10^{-25} \text{ cm}^3 \text{ s}^{-1}$ to characterise the region of overlap for the various excesses, and made use of only a 3 arcminute observation region and scaled point source sensitivity for MeerKAT. We found that 5σ detection is possible, within 20 hours of ob-

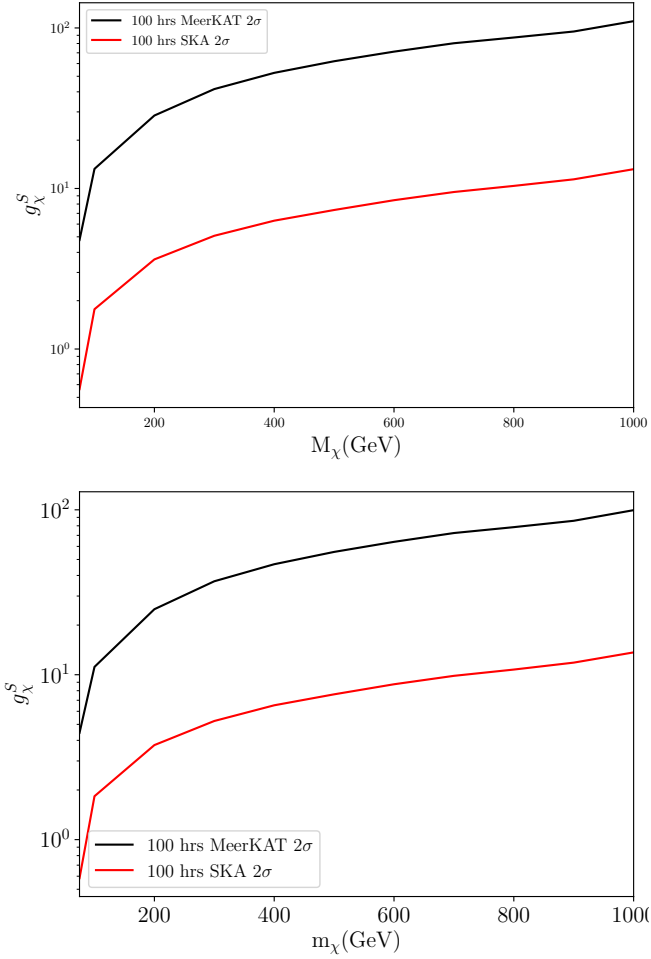


Figure 7. Non-observation 2σ exclusion projections on the coupling between S and χ ($2 \rightarrow 2$ case) for Reticulum II (Einasto profile) with MeerKAT and the SKA. *Top:* Milky-Way galactic centre with Einasto profile. *Bottom:* Milky-Way galactic centre with NFW profile.

servation at lower masses. However, around 1000 hours might be necessary to survey up to 200 GeV. This would still fail to cover the entire uncertainty region, so some of the parameter space can evade any conceivable detection with MeerKAT. This is not the case with the full SKA. Which, at 5σ confidence interval and 100 hours observing time, can probe the entire uncertainty band for all masses in the excess overlap window. However, we note that an optimised MeerKAT search for diffuse emissions will likely have increased sensitivity.

It is worth highlighting that the MeerKAT sensitivity estimates have highly competitive constraining power, even somewhat exceeding that of Fermi-LAT data. MeerKAT can explore a significant area of the full excess overlap parameter space at 2σ confidence level with 100 hours of observing time. Whereas, Fermi-LAT with data from [Albert et al. \(2017\)](#) and a 10 times larger integration radius does not intrude at all upon these parameter regions. On the other hand, the full SKA can explore the entire overlap parameter space, even within uncertainties due to ρ_\odot , with less than 100 hours of observation. However, at present MeerKAT will be the fron-

tier in radio instruments for DM searches, especially since it has begun observing calls already and will be upgraded in the near future with 30% more dishes.

The results documented in this work have implications on searches for DM at the LHC, due to the fact that limits on the cross-section from $\chi\chi \rightarrow \text{SM}$ translate directly to the coupling between χ and S in Eq. (4), as the other model parameters are fixed. Additionally, as an SM singlet, S is predominantly produced via the decay of the heavy scalar $H \rightarrow SS$. Thus, DM produced via the decay of S can recoil against SM particles that S can also decay into ([von Buddenbrock et al. 2016](#)). Of particular interest would be the resonant search for $S \rightarrow ZZ, Z\gamma, \gamma\gamma$ in association with moderate missing transverse energy carried by the DM. The astrophysical data provides a consistency test as well as a narrowed region of focus, in which collider data can be used to further probe the properties of 2HDM+ S with respect to its unconstrained degrees of freedom.

ACKNOWLEDGMENTS

The authors want to thank Andreas Crivellin and Bhupal Dev for most useful discussions. The authors are grateful for support from the South African Department of Science and Innovation through the SA-CERN program and the National Research Foundation for various forms of support. GB acknowledges the funding of the National Research Foundation through Thuthuka grant number 117969.

REFERENCES

- Aad G., et al., 2012, [Phys. Lett. B](#), 716, 1
- Aad G., et al., 2013, [Phys. Lett. B](#), 726, 120
- Ackermann M., et al., 2017, [The Astrophysical Journal](#), 840, 43
- Adams J. J., et al., 2014, [ApJ](#), 789, 63
- Aghanim N., et al., 2020, [Astronomy & Astrophysics](#), 641, A6
- Aguilar M., et al., 2016, [Phys. Rev. Lett.](#), 117, 091103
- Aguilar M., et al., 2019, [Phys. Rev. Lett.](#), 122, 041102
- Albert A., et al., 2017, [The Astrophysical Journal](#), 834, 110
- Alwall J., Herquet M., Maltoni F., Mattelaer O., Stelzer T., 2011, [JHEP](#), 06, 128
- Atwood W., et al., 2009, [The Astrophysical Journal](#), 697, 1071
- Baltz E. A., Edsjö J., 1998, [Physical Review D](#), 59, 023511
- Baltz E. A., Wai L., 2004, [Physical Review D](#), 70, 023512
- Bechtol K., et al., 2015, [ApJ](#), 807, 50
- Beck G., 2019, [Journal of Cosmology and Astroparticle Physics](#), 2019, 019–019
- Beck G., Colafrancesco S., 2016, [JCAP](#), 1605, 013
- Bell N. F., Busoni G., Sanderson I. W., 2017, [JCAP](#), 03, 015
- Benito M., Cuoco A., Iocco F., 2019, [Journal of Cosmology and Astroparticle Physics](#), 2019, 033–033
- Booth R. S., de Blok W. J. G., Jonas J. L., Fanaroff B., 2009, MeerKAT Key Project Science, Specifications, and Proposals ([arXiv:0910.2935](#))
- Braun R., Bonaldi A., Bourke T., Keane E., Wagg J., 2019, Anticipated Performance of the Square Kilometre Array – Phase 1 (SKA1) ([arXiv:1912.12699](#))
- Buddenbrock S., Cornell A. S., Fang Y., Fadol Mohammed A., Kumar M., Mellado B., Tomiwa K. G., 2019a, [JHEP](#), 10, 157
- Buddenbrock S., Cornell A. S., Fang Y., Fadol Mohammed A., Kumar M., Mellado B., Tomiwa K. G., 2019b, [JHEP](#), 10, 157
- Chatrchyan S., et al., 2012, [Phys. Lett. B](#), 716, 30
- Chatrchyan S., et al., 2013, [Phys. Rev. Lett.](#), 110, 081803

- Cholis I., Linden T., Hooper D., 2019, *Physical Review D*, 99
- Cirelli M., et al., 2011, *JCAP*, 1103, 051
- Colafrancesco S., Profumo S., Ullio P., 2006, *Astronomy and Astrophysics*, 455, 21
- Colafrancesco S., Profumo S., Ullio P., 2007, *Physical Review D*, 75, 023513
- Colafrancesco S., Marchegiani P., Beck G., 2015, *JCAP*, 02, 032C
- Crivellin A., et al., 2021, Accumulating Evidence for the Associate Production of a Neutral Scalar with Mass around 151 GeV ([arXiv:2109.02650](https://arxiv.org/abs/2109.02650))
- Das A., Dasgupta B., Ray A., 2020, *Phys. Rev. D*, 101, 063014
- Dewdney P., Turner W., Millenaar R., McCool R., Lazio J., Cornwell T., 2012, SKA baseline design document
- Di Mauro M., 2021, *Physical Review D*, 103, 063029
- Egorov A. E., Pierpaoli E., 2013, *Physical Review D*, 88, 023504
- Einasto J., 1968, Publications of the Tartuskoj Astrofizica Observatory, 36, 414
- Englert F., Brout R., 1964, *Phys. Rev. Lett.*, 13, 321
- Fang K., Bi X.-J., Yin P.-F., 2019, *The Astrophysical Journal*, 884, 124
- Farzan Y., Rajaei M., 2019, *Journal of Cosmology and Astroparticle Physics*, 2019, 040
- Fischer O., et al., 2022, *The European Physical Journal C*, 82
- Giesen G., Boudaud M., Génolini Y., Poulin V., Cirelli M., Salati P., Serpico P. D., 2015, *Journal of Cosmology and Astroparticle Physics*, 2015, 023–023
- Guralnik G. S., Hagen C. R., Kibble T. W. B., 1964, *Phys. Rev. Lett.*, 13, 585
- Heisig J., Korsmeier M., Winkler M. W., 2020, *Physical Review Research*, 2
- Hernandez Y., et al., 2021, *Eur. Phys. J. C*, 81, 365
- Higgs P. W., 1964a, *Phys. Lett.*, 12, 132
- Higgs P. W., 1964b, *Phys. Rev. Lett.*, 13, 508
- Hoekstra H., Yee H., Gladders M. D., 2002, *New Astronomy Reviews*, 46, 767–781
- Ishiwata K., Macias O., Ando S., Arimoto M., 2020, *Journal of Cosmology and Astroparticle Physics*, 2020, 003
- Koopmans L. V. E., Treu T., 2003, *The Astrophysical Journal*, 583, 606–615
- Koposov S. E., Belokurov V., Torrealba G., Evans N. W., 2015, *ApJ*, 805, 130
- Li T., 2018, *Journal of High Energy Physics*, 2018
- Longair M. S., 1994, *High Energy Astrophysics*. Cambridge University Press
- Marr J., Snell R., Kurtz S., 2015, *Fundamentals of Radio Astronomy: Observational Methods*. CRC Press
- Maurin D., Donato F., Taillet R., Salati P., 2001, *The Astrophysical Journal*, 555, 585
- Mauro M. D., Donato F., Fornengo N., Vittino A., 2016, *Journal of Cosmology and Astroparticle Physics*, 2016, 031–031
- Metcalf R. B., Moustakas L. A., Bunker A. J., Parry I. R., 2004, *The Astrophysical Journal*, 607, 43–59
- Moustakas L. A., Metcalf R. B., 2003, *Monthly Notices of the Royal Astronomical Society*, 339, 607–615
- Navarro J. F., Frenk C. S., White S. D. M., 1996, *The Astrophysical Journal*, 462, 563
- Profumo S., Queiroz F., Siqueira C., 2020, *J. Phys. G*, 48, 015006
- Regis M., Colafrancesco S., Profumo S., de Blok W., Massardi M., Richter L., 2014, *Journal of Cosmology and Astroparticle Physics*, 2014, 016–016
- Regis M., Richter L., Colafrancesco S., 2017, *Journal of Cosmology and Astroparticle Physics*, 2017, 025
- Rybicki G. B., Lightman A. P., 1986, *Radiative Processes in Astrophysics*. Wiley
- Sabatta D., Cornell A. S., Goyal A., Kumar M., Mellado B., Ruan X., 2020, *Chin. Phys. C*, 44, 063103
- Sjöstrand T., Mrenna S., Skands P., 2008, *Computer Physics Communications*, 178, 852–867
- Steigman G., Dasgupta B., Beacom J. F., 2012, *Phys. Rev.*, D86, 023506
- Walker M. G., Mateo M., Olszewski E. W., Narrubia J. P., Evans N. W., Gilmore G., 2009, *ApJ*, 704, 1274
- Weber M., de Boer W., 2010, *Astronomy and Astrophysics*, 509, A25
- von Buddenbrock S., et al., 2016, *Eur. Phys. J. C*, 76, 580
- von Buddenbrock S., Cornell A. S., Fadol A., Kumar M., Mellado B., Ruan X., 2018, *J. Phys. G*, 45, 115003
- von Buddenbrock S., Cornell A. S., Iarilala E. D. R., Kumar M., Mellado B., Ruan X., Shrif E. M., 2019, *J. Phys. G*, 46, 115001
- von Buddenbrock S., Ruiz R., Mellado B., 2020, *Phys. Lett. B*, 811, 135964